Atmos. Chem. Phys. Discuss., 15, 6373–6401, 2015
www.atmos-chem-phys-discuss.net/15/6373/2015/
doi:10.5194/acpd-15-6373-2015

Atmospheric Chemistry and Physics Discussions

Tropospheric ozone variability in the tropics from ENSO to MJO and shorter timescales

J. R. Ziemke[1,2], A. R. Douglass[2], L. D. Oman[2], S. E. Strahan[2,3], and B. N. Duncan[2]

[1]Morgan State University, Baltimore, Maryland, USA
[2]NASA Goddard Space Flight Center, Greenbelt, Maryland, USA
[3]Universities Space Research Association, Columbia, Maryland, USA

Received: 8 December 2014 – Accepted: 9 February 2015 – Published: 5 March 2015

Correspondence to: J. R. Ziemke (jerald.r.ziemke@nasa.gov)

Published by Copernicus Publications on behalf of the European Geosciences Union.

Abstract

Aura OMI and MLS measurements are combined to produce daily maps of tropospheric ozone beginning October 2004. We show that El Ni no Southern Oscillation (ENSO) related inter-annual change in tropospheric ozone in the tropics is small compared to combined intra-seasonal/Madden–Julian Oscillation (MJO) and shorter timescale variability by a factor ∼ 3–10 (largest in the Atlantic). Outgoing Longwave Radiation (OLR) indicates further that deep convection is the primary driver of the observed tropospheric ozone variability from ENSO down to weekly timescales. We compare tropospheric ozone and OLR satellite observations with two simulations: (1) the Goddard Earth Observing System (GEOS) chemistry-climate model (CCM) that uses observed sea surface temperatures and is otherwise free-running, and (2) the NASA Global Modeling Initiative (GMI) chemical transport model (CTM) that is driven by Modern-Era Retrospective Analysis for Research and Applications (MERRA) analyses. It is shown that the CTM-simulated ozone accurately matches measurements for timescales from ENSO to intra-seasonal/MJO and even 1–2 week periods; however (though not unexpected) the CCM simulation reproduces ENSO variability but not shorter timescales. These analyses suggest that using a model to delineate temporal/spatial properties of tropospheric ozone and convection in the tropics will require that the model reproduce the non-ENSO variability that dominates.

1 Introduction

The El Niño Southern Oscillation (ENSO) and its effects on the atmosphere and ocean have been extensively studied and documented. Trenberth (1997) provides several key references with an overview description and historical account of ENSO. The terminology, "ENSO", is understood to consist of El Niño (warmer than average ocean temperatures in the tropical eastern Pacific – i.e., "warm phase") typically followed by La Niña (cooler than average ocean temperatures in the tropical eastern Pacific – i.e.,

ACPD
15, 6373–6401, 2015

"cool phase"). ENSO events have ~ 2–7 year timescales and produce planetary-scale changes in tropical sea surface temperature (SST), convection, and winds. Peak activity for ENSO occurs generally centered about Northern Hemisphere autumn to mid-winter months (e.g., largely October–January).

The effects of El Niño on atmospheric composition, including ozone, have been studied from both satellite and ground-based measurements (e.g., Chandra et al., 1998; Fujiwara et al. 1999; Thompson et al., 2001; Lee et al., 2010; Ziemke et al., 2010; Randel and Thompson, 2011), global chemical transport models driven by specified meteorology (e.g., Duncan et al., 2003; Chandra et al., 2009) and general circulation models (GCMs) (e.g., Sudo and Takahashi, 2001; Zeng and Pyle, 2005; Doherty et al., 2006; Randel et al., 2009; Oman et al., 2011). Tropospheric ozone is important as both a greenhouse gas and precursor of the hydroxyl radical (OH), the primary atmospheric oxidant. Tropospheric ozone in the tropics is especially sensitive to changes in deep convection associated with ENSO. An increase (decrease) in dynamical convection from ENSO events in the tropical Pacific induces a decrease (increase) in tropospheric column ozone. Although changes in convection are fundamentally dynamical there are also ENSO-related changes in composition that affect ozone precursors, such as increases in emissions from biomass burning over Indonesia due to suppressed rainfall during El Niño. There can also be long-range transport effects on tropospheric ozone related to ENSO including induced trends over long records. Lin et al. (2014) studied the effects of ENSO/Pacific Decadal Oscillation (PDO) on tropospheric ozone at the Mauna Loa Observatory (19.5° N, 155.6° W; altitude 3.4 km). By combining 40 years of surface ozone measurements with a set of chemistry-climate model simulations they found that the multi-decadal positive trend measured in tropospheric ozone during autumn months (September–October) at Mauna Loa could be explained from an increase in transport of Asian pollution.

Ziemke et al. (2010) produced a monthly tropospheric ozone ENSO index (OEI) over a multi-decadal time record (beginning 1979) by differencing satellite-measured column ozone in the tropics between the eastern and western Pacific. They noted that the OEI

ACPD
15, 6373–6401, 2015

could be used as a diagnostic test for modeled ozone including tropospheric ozone sensitivity relating to changes in SSTs. Oman et al. (2011) found excellent agreement between the measured OEI with the OEI produced by the Goddard Earth Observing System (GEOS) free-running chemistry-climate model (CCM) with observed SSTs over a 25 year period. This demonstrated an appropriate response of the CCM meteorology to the ENSO signature of the imposed SSTs; the fidelity of the ozone response to the induced circulation and photochemical changes included realistic horizontal and vertical gradients in tropospheric ozone.

The tropical atmosphere exhibits intra-seasonal and shorter timescale variability with periods much shorter than ENSO from days or weeks to several months. In the tropical Indian Ocean and western Pacific the leading source of intra-seasonal variability is related to the Madden–Julian Oscillation (MJO) with characteristic timescales of about 1–2 months (Madden and Julian, 1971, 1994). Like ENSO, the MJO influences tropical air and SSTs, winds, convection and rainfall, and other important aspects of the weather and climate system. The strongest MJO variability occurs around northern wintertime months when the intensity of ENSO events is largest. The MJO modulates regional monsoon, thereby impacting air quality in the tropics/subtropics involving particulate matter (e.g., Ragsdale et al., 2013) and surface ozone (e.g., Barrett et al.., 2012). The MJO with its associated ocean–atmosphere coupling may affect the duration and onset of ENSO (e.g., Hoell et al., 2014, and references therein). The MJO also alters stratospheric circulation including stratospheric sudden warming events (e.g., Garfinkel et al., 2012, 2014, and references therein) and modulation of tropical Kelvin waves (Guo et al., 2014).

Using a chemical transport model (CTM) and measurements from the Aura Tropospheric Emission Spectrometer (TES) instrument, Sun et al. (2014) indicated that the MJO in tropospheric ozone in tropical latitudes may be locally up to 47 % of total variability. Their estimate is comparable to the ∼ 5–10 Dobson Units (DU; 1 DU = 2.69×10^{20} molecules m^{-2}) MJO variability (out of ∼ 15–20 DU background ozone) in troposphere ozone in the tropical Pacific by Ziemke and Chandra (2003). In addition

ACPD
15, 6373–6401, 2015

to ENSO and intra-seasonal/MJO changes, Dunkerton and Crum (1995) showed that there is considerable convective variability in the tropics with shorter timescales such as 2–15 days. Dunkerton and Crum (1995) used daily outgoing longwave radiation (OLR) in the tropics to relate 2–15 day disturbances with intra-seasonal oscillations/MJO signals and found distinction between them as well as moderate interaction between them during convectively active phases of the intra-seasonal oscillations. A long existing problem with GCM/CCM simulations is difficultly in producing a realistic MJO in the atmosphere. Efforts have demonstrated however that there is a causal link between how well gross moist stability and vertical advection is treated in models with how well these models can reproduce a variation similar to the MJO (e.g., Benedict et al., 2014, and references therein).

The purpose of our study is to characterize the variability of tropical tropospheric ozone for timescales ranging from ENSO to MJO and shorter time periods in relation to tropical convection and atmospheric model simulations of ozone. We compare observed tropospheric ozone with ozone simulated from two NASA Goddard models of atmospheric composition, one being a CCM forced by observed monthly SSTs and the other a CTM driven by meteorological analyses. Section 2 discusses data and models for our analysis while Sect. 3 describes the impact of ENSO vs. non-ENSO related changes in tropospheric ozone in relation with convective forcing. Section 4 describes derivation of a useful tropospheric ozone diagnostic from OMI/MLS while Sect. 5 shows some of its applications as applied to model ozone and OLR measurements. Section 6 finally provides a summary.

2 Data and models

Daily measurements of tropospheric column ozone (TCO) in tropical latitudes are calculated using the OMI/MLS residual method of Ziemke et al. (2006). This method subtracts MLS stratospheric column ozone (SCO) from OMI total column ozone for near clear-sky scenes (i.e., radiative cloud fractions < 30 %). Ziemke et al. (2014) evalu-

ACPD
15, 6373–6401, 2015

ated three other OMI/MLS tropospheric ozone products and concluded that the Global Modeling and Assimilation Office (GMAO) data assimilation product was deemed best to use overall when considering all factors including global coverage and ozone profile information. However, Fig. 12 of Ziemke et al. (2014) showed that the assimilation product when limited to only tropical latitudes had a zonal wave structure ~ 10–15 DU in seasonally averaged SCO which was considerably larger than direct satellite measurements that typically have only a few DU zonal variability for monthly means. In addition, this larger zonal variability in SCO with assimilation coincided with reduced zonal variability of TCO, also considered inconsistent with previous TCO measurements.While all of the OMI/MLS daily products compare favorably with ozonesondes in the tropics, we use the product of Ziemke et al. (2006) which was found to be the most consonant with OLR measurements and the CTM over all timescales. This residual product combines MLS v3.3 ozone profiles with OMI version 8.5 total ozone measurements. Data quality and description of the MLS v3.3 ozone profiles are discussed by Livesey et al. (2011). Description and access to the OMI data may be obtained from the NASA webpage http://disc.sci.gsfc.nasa.gov/Aura/data-holdings/OMI. Horizontal gridding for TCO is 1° latitude × 1.25° longitude. The OMI/MLS residual ozone product uses WMO NCEP 2 K km^{-1} lapse-rate tropopause pressure to separate tropospheric from stratospheric ozone. Our study also uses OLR daily measurements for 2004–2012 at 2.5° × 2.5° horizontal gridding obtained from the National Oceanic and Atmospheric Administration (NOAA) webpage http://www.esrl.noaa.gov/psd/data/gridded/.

The Global Modeling Initiative (GMI) CTM hindcast simulation includes a chemical mechanism suitable for the troposphere and stratosphere (Duncan et al., 2008; Strahan et al., 2007). The emissions of trace gases and aerosol fields used in the CTM simulations are described by Duncan et al. (2008), however, anthropogenic emissions have been updated since Duncan et al. (2008) and include year-specific scaling factors (van Donkelaar et al., 2008). Anthropogenic and biomass global emissions include surface emissions from industry/fossil fuel, biomass burning, biofuel combustions, and contributions from aircraft. Biomass burning emissions in the CTM are from

ACPD
15, 6373–6401, 2015

van der Werf et al. (2010) and are extended through year 2010. Observationally-based biomass burning emissions are used in the CTM for years 2004 through 2010 with the 2010 emissions repeated for each year 2011–2012. More detailed description of emissions for this simulation is given by Strode et al. (2014). The CTM meteorological fields are taken from Modern-Era Retrospective Analysis for Research and Applications (MERRA) analyses (Rienecker et al., 2011).

The CCM is described by Oman et al. (2013). This CCM is forced by observed monthly SSTs and specified boundary conditions and fluxes of important greenhouse gases including carbon dioxide, methane, and nitrous oxide. The CCM uses observed monthly mean SSTs over the 1960–2012 time record and uses the same biomass burning emissions as described here for the CTM.

3 ENSO vs. non-ENSO timescale changes in tropospheric ozone

Variability of tropospheric ozone from OMI/MLS and the CTM is shown in Fig. 1 for ENSO, non-ENSO, and intra-seasonal oscillation (ISO) timescale changes. Also plotted in Fig. 1 are corresponding calculations for OLR, scaled downward by a factor of 5 for plotting with ozone. ENSO signals (bottom curves) were extracted from original deseasonalized ozone and OLR time series using the linear regression $T(t) = \beta \cdot \mathrm{Nino34}(t-1) + \varepsilon(t)$, where T is original time series, t is day index, β is a derived constant, Nino34(t) is the Nino 3.4 ENSO index, and $\varepsilon(t)$ is the residual. All line curves in Fig. 1 represent 20° S–20° N averages as function of longitude. The ISO variability (middle curves) involved band-pass filtering original time series for 25–65 day periods.

ENSO contributes a relatively small amount to the total daily variability of tropospheric ozone in the tropics. Figure 1 shows that ENSO related change in tropospheric ozone and convection (bottom curves) is smaller than either non-ENSO change (top curves) or ISO timescale changes (middle curves). The CTM reproduces all of the OMI/MLS tropospheric ozone patterns for all three timescale scenarios. Most of the non-ENSO related changes involve the intra-seasonal/MJO and shorter time period

ACPD
15, 6373–6401, 2015

changes. These are larger than ENSO by a factor of ∼ 3–4 in the Pacific and a factor of 10 or more in the Atlantic.

4 The daily ozone dipole index (ODI)

We calculate a quantity that we refer to as the ozone dipole index (ODI). This differs from the monthly OEI used by Ziemke et al. (2010) in that it is calculated using daily measurements rather than monthly means and does not include the final 3 month running average that is applied to the OEI. We use this ODI as a diagnostic test for evaluating OMI/MLS tropospheric ozone with other atmospheric parameters, including satellite measured OLR and similar troposphere ozone derived from models. The ODI is the deseasonalized difference of western minus eastern Pacific TCO time series each day over the Aura record. The ODI calculation involves first averaging TCO from OMI/MLS each day in the tropics over the broad eastern and western Pacific regions (i.e., 15° S–15° N, 110–180° W and 15° S–15° N, 70–140° E, respectively). As with the monthly OEI, the differencing removes measurement offsets or drifts with time that would be common to both Pacific time series. We also calculate a daily dipole index time series for National Oceanic and Atmospheric Administration (NOAA) OLR measurements in the same manner as calculation of the ODI for investigating connections between tropospheric ozone and convection.

Statistical coherence and phase of coherence are calculated between the measured ODI and the ODI's derived from the CTM and CCM. These statistics are also calculated between the measured ODI and the OLR daily dipole series. Coherence, a normalized statistic with values lying between zero and 1.0, provides evaluation of statistical connection between two time series as an explicit function of frequency. We refer the reader to Appendix A for details regarding these calculations.

ACPD
15, 6373–6401, 2015

5 Comparisons between measured and modeled ODI

In Fig. 2a we compare time series of measured ODI (red curve) and CTM ODI (dotted blue curve). The two time series appear remarkably similar for timescales varying from low frequency ENSO to 1–2 month periods (e.g., MJO) and even shorter. Figure 2b is the same as Fig. 2a but for the CCM instead of CTM. The CCM in Fig. 2b reproduces ENSO variability and appears to produce variability with appropriate magnitudes for shorter timescales.

We calculate coherence and coherence-phase as functions of frequency to establish the statistical connection between measured and simulated ODI's on varying timescales. The coherence and coherence-phase calculated between the OMI/MLS and CTM ODI's are shown in Fig. 3a where square of coherence is shown in the top panel with coherence-phase on the bottom. Time periods in days are printed along the horizontal frequency axes for all panels in Fig. 3.

If a simulated ODI exactly matched that obtained from OMI/MLS then the squared coherence would be 1.0 over the entire frequency spectrum and the phase shift would be zero. For the CTM in Fig. 3a, statistical significance of squared coherence exceeds the 99 % level for values greater than 0.684. The CTM squared coherence exceeds this value for a broad range of timescales from ENSO (at far left in panel) to the MJO (30–60 days), down to timescales as short as 7–14 days. The excellent agreement in Fig. 3a over broad timescales attests to the realism of the input meteorology and computed photochemistry within the CTM. Figure 3b shows similar calculations for the CCM. The squared coherence in Fig. 3b (top) is statistically significant for ENSO but not shorter timescales. In addition the phase between OMI/MLS and the CCM in Fig. 3b (bottom) is near zero only for very low-frequency ENSO variability.

OLR is well known as a proxy of cloudiness where high OLR corresponds to deep convection. Comparison of the OMI/MLS ODI with the OLR dipole series in Fig. 4 shows that convection is the fundamental driver of tropospheric ozone variability in the tropical Pacific from ENSO to MJO and shorter periods. OLR indicates that convec-

ACPD
15, 6373–6401, 2015

tion in the MERRA analyses is being accurately simulated from ENSO down to short timescales.

Figure 5 compares calculated spectral amplitudes of the ODI obtained from OMI/MLS data (red curve), CTM output (blue dotted curve), and CCM output (green dashed curve). The spectral amplitudes for OMI/MLS and the CTM in Fig. 5 are everywhere comparable and the variability shown by peaks and valleys as functions of frequency are closely identical for periods even shorter than ~ 30 days. In comparison, the CCM has considerably smaller amplitudes at all frequencies and the frequency variability of spectral amplitudes is not consistent with the observations. The spectral analysis including the coherence/coherence-phase statistics for the CCM shows that visual inspection alone to compare time series or simple statistics (such as calculated RMS numbers) is not sufficient to evaluate model performance.

Power spectra for TCO time series averaged over the Indian Ocean just north of the equator are shown in Fig. 6 for OMI/MLS ozone and the CTM and CCM simulated ozone. This tropical region is where the 1–2 month MJO signal-to-noise in tropical TCO maximizes for both data and the CTM. MJO variability in Fig. 5 has well defined peak amplitudes around 45–50 day period for both the data and the CTM. However the CCM power spectrum does not show any consistent MJO or shorter timescale variability and essentially only generates an ENSO variation at very low frequency.

6 Summary

We have studied the variability of tropospheric ozone in the tropics from ENSO to intraseasonal/MJO and weekly timescales using satellite measurements and two simulation models. Aura OMI and MLS satellite measurements are combined to derive daily maps of tropospheric ozone for October 2004 through 2012. Daily OLR from NOAA for the same time record are included to relate tropospheric ozone variability to changes in convection. The two models that we use are (1) the free-running GEOS Chemistry-Climate Model (CCM) and (2) the Global Modeling Initiative (GMI) chemistry-transport

ACPD
15, 6373–6401, 2015

model (CTM) driven by Modern-Era Retrospective Analysis for Research and Applications (MERRA) meteorological analyses.

Non-ENSO timescale changes in measured tropospheric ozone and convection in the tropics are found to be substantially larger than ENSO related changes by a factor of about 3–4 in the Pacific and up to a factor of 10 or more in the Atlantic. This non-ENSO variability in tropospheric ozone and convection is comprised mostly of intra-seasonal/MJO to 1–2 week timescale changes. Time series analysis including coherence calculations with OLR satellite data indicate that tropospheric ozone variability from ENSO down to weekly timescales in the tropics is driven primarily by convection.

We developed a tropospheric ozone dipole index (ODI) from OMI/MLS measurements by differencing western minus eastern Pacific tropospheric column ozone time series. The ODI is demonstrated to be a useful diagnostic for testing model ozone variability from ENSO down to weekly timescales. The ODI is derived similar to the monthly-mean Ozone ENSO Index (OEI) of Ziemke et al. (2010), but instead using daily measurements. The ODI was compared with ODI calculated from both the CTM and CCM. It is shown that the ODI obtained from the CTM is highly coherent with the measured ODI for timescales varying from ENSO to 1–2 month MJO and even shorter weekly time periods. The remarkable coherent behavior between the CTM ODI and measured ODI attests to the accuracy of the MERRA analyses and also that the CTM largely combines the effects of dynamics and photochemistry correctly over this broad range of timescales.

Our analyses show that the Goddard CTM reproduces ozone observations exceptionally well over time scales from ENSO down to weekly periods whereas the Goddard CCM reproduces only ENSO variability. The inability of the CCM to generate shorter time scales is a known problem with GCMs/CCMs. Understanding the differences in ozone variability between the CCM and CTM can help quantify possible missing or inaccurate feedback processes as future work. An important result we find is that using a model to quantify temporal and spatial properties of tropospheric ozone in the tropics requires that the model properly simulate the dominant non-ENSO variability.

ACPD
15, 6373–6401, 2015

Appendix A:

A1 Estimated precision errors for OMI/MLS TCO including calculated ODI

Estimated RMS precision errors for OMI/MLS 1° × 1.25° daily gridded TCO are given by Kar et al. (2010). Precision values in the extra-tropics were shown to be up to ~ 10 DU or greater while in tropical latitudes values were smaller at ~ 5 DU. Figure A1 shows daily time series of eastern and western Pacific OMI/MLS TCO used to calculate the ODI (the two Pacific regions are defined in the figure caption). The ODI follows by taking the western minus eastern Pacific TCO each day followed by deseasonalizing this difference time series (deseasonalization is discussed in Sect. A2 below). The time series in Fig. A1 appear generally of opposite signature with evidence of some temporal phase shifts for intra-seasonal and shorter timescales. An El Niño (La Niña) condition coincides when these two time series have largest (smallest) separation on inter-annual timescale.

RMS precision errors for the time series in Fig. A1 were obtained by taking local daily RMS uncertainties at 1° × 1.25° resolution and adjusting these numbers by the spatial averaging invoked. By taking an upper bound of 10 DU for this number and dividing it by $\sqrt{N}$ (N is the total number of the grid points included in the spatial averaging) we get an estimate of time series precision. (This precision estimate represents standard error of the mean.) Dividing by $\sqrt{N}$ assumes that tropospheric ozone measurements detected by OMI are stochastically independent. For either the western or eastern Pacific region encompassing a domain of 30° latitude × 70° longitude there are a total of 1680 grid points. Largely because of applied cloud filtering (i.e., cloud fractions < 30 %) the actual average number of grid points is about 680 (i.e., N = 680). This yields $10/\sqrt{680}$ = 0.38 DU as an estimated precision for either eastern or western Pacific time series in Fig. A1. An estimate of precision for the daily ODI is then $\sqrt{0.38^2 + 0.38^2}$ = 0.54 DU assuming stochastic independence between the two regions.

ACPD
15, 6373–6401, 2015

A2 Spectral analysis

Koopmans (1974) details calculation of coherence and its phase using Fourier spectral analysis with smoothed spectral estimators. All daily ozone time series in our study were deseasonalized prior to any Fourier analysis. Deseasonalization was accomplished by first applying a low-pass filter (with half-amplitude filter response at 60 day period and zero phase shift at all periods) to original daily time series; this was followed by averaging similar days over consecutive years to obtain a 365 day pseudo-climatology for the annual cycle. This estimated annual climatology was then subtracted from original daily time series for each consecutive year. Potential leakage of nearby Fourier cosine and sine coefficients was reduced by applying a tapered cosine window to deseasonalized time series with 25 % cosine tapering at each end (e.g., Harris, 1978). For all derived spectra including cross-spectra for coherence we applied a Daniell 7-point smoothed spectral estimator. Resulting critical coherence at 95, 99 %, and 99.9 % confidence levels is 0.627, 0.732, and 0.827, respectively.

Power spectra with estimated 1–2 month signal-to-noise was calculated in the tropics for OMI/MLS and CTM TCO similar to Ziemke et al. (2007). Figure 6. in the main text shows power spectra with estimated signal-to-noise for both background and 1–2 months signals for the Indian Ocean region where the MJO signal for both OMI/MLS and CTM TCO is largest. In Fig. 6, estimated background noise power spectra (i.e., denoted "BG") for each time series was estimated using a first-order autoregressive model $T(t) = \alpha \cdot T(t-1) + N(t)$, where α is a derived constant, t is the day index, and $N(t)$ is normally distributed random noise with mean of zero. For power spectra using the 7-point estimator the 95 % critical signal-to-noise ratio level is 1.69.

A3 ENSO vs. non-ENSO variability

The top panel in Fig. A2 shows OMI/MLS time series for the ENSO component (thick curve), non-ENSO component (thin curve), and annual cycle (dotted curve) in the tropical western Pacific. The bottom panel in Fig. A2 is the same as the top panel but

ACPD
15, 6373–6401, 2015

instead for the CTM. The selected region for these time series is 10–20° S, 115–120° E which coincides with largest ENSO variability for both OMI/MLS and CTM TCO. The ENSO variability was extracted using linear regression (see figure caption). Figure A2 shows that the CTM closely tracks OMI/MLS measurements for the non-ENSO components. ENSO variability for both the CTM and OMI/MLS is smaller than non-ENSO (comprised mostly of MJO and shorter timescales).

Acknowledgements. The authors thank the Aura MLS and OMI instrument and algorithm teams for the extensive satellite measurements used in this study. OMI is a Dutch-Finnish contribution to the Aura mission. The authors also thank the modeling teams and their efforts involving the NASA CCM and CTM results. Funding for this research was provided in part by NASA NN10ZDA001N-AURA.

References

Barrett, B. S., S. J. Fitzmaurice, and Pritchard, S. R.: Intraseasonal variability of surface ozone in Santiago, Chile: modulation by phase of the Madden–Julian Oscillation (MJO), Atmos. Environ., 57, 55–62, doi:10.1016/j.atmosenv.2012.04.040, 2012.

Benedict, J. J., Maloney, E. D., Sobel, A. H., and Frierson, D. M. W.: Gross moist stability and MJO simulations skill in three full-physics GMSs, J. Geophys. Res., 71, 3327–3349, doi:10.1175/JAS-D-13-0240.1, 2014.

Chandra, S., Ziemke, J. R., Min, W., and Read, W. G.: Effects of 1997–1998 El Niño on tropospheric ozone and water vapor, Geophys. Res. Lett., 25, 3867–3870, doi:10.1029/98GL02695, 1998.

Chandra, S., Ziemke, J. R., Duncan, B. N., Diehl, T. L., Livesey, N. J., and Froidevaux, L.: Effects of the 2006 El Niño on tropospheric ozone and carbon monoxide: implications for dynamics and biomass burning, Atmos. Chem. Phys., 9, 4239–4249, doi:10.5194/acp-9-4239-2009, 2009.

Doherty, R. M., Stevenson, D. S., Johnson, C. E., Collins, W. J., and Sanderson, M. G.: Tropospheric ozone and El Niño–Southern Oscillation: influence of atmospheric dynamics, biomass burning emissions, and future climate change, J. Geophys. Res., 111, D19304, doi:10.1029/2005JD006849, 2006.

ACPD
15, 6373–6401, 2015

Duncan, B. N., Martin, R. V., Staudt, A., Yevich, R., and Logan, J. A.: Inter-annual and seasonal variability of biomass burning emissions constrained by satellite observations, J. Geophys. Res., 108, 4100, doi:10.1029/2002JD002378, 2003.

Duncan, B. N., West, J. J., Yoshida, Y., Fiore, A. M., and Ziemke, J. R.: The influence of European pollution on ozone in the Near East and northern Africa, Atmos. Chem. Phys., 8, 2267–2283, doi:10.5194/acp-8-2267-2008, 2008.

Dunkerton, T. J. and Crum, F. X.: Eastward propagating ∼2- to 15-day equatorial convection and its relation to the tropical intraseasonal oscillation, J. Geophys. Res., 100, 25781–25790, doi:10.1029/95JD02678, 1995.

Fujiwara, M., Kita, K., Kawakami, S., Ogawa, T., Komala, N., Saraspriya, S., and Suripto, A.: Tropospheric ozone enhancements during the Indonesian forest fire events in 1994 and in 1997 as revealed by ground-based observations, Geophys. Res. Lett., 26, 2417–2420, doi:10.1029/1999GL900117, 1999.

Garfinkel, C. I., Feldstein, S. B., Waugh, D. W., Yoo, C., and Lee, S.: Observed connection between stratospheric sudden warmings and the Madden–Julian Oscillation, Geophys. Res. Lett., 39, L18807, doi:10.1029/2012GL053144, 2012.

Garfinkel, C. I., Benedict, J. J., and Maloney, E. D.: Impact of the MJO on the boreal winter extra-tropical circulation, Geophys. Res. Lett., 41, 6055–6062, doi:10.1002/2014GL061094, 2014.

Guo, Y. J., Jiang, X. A., and Waliser, D. E.: Modulation of the convectively coupled Kelvin waves over South America and the tropical Atlantic Ocean in association with the Madden–Julian Oscillation, J. Atmos. Sci., 71, 1371–188, doi:10.1175/JAS-D-13-0215.1, 2014.

Harris, F.: On the use of windows for harmonic analysis with the discrete Fourier transform, P. IEEE, 66, 51–83, 1978.

Hoell, A., Barlow, M., Wheeler, M. C., and Funk, C.: Disruptions of El Niño – southern oscillation teleconnections by the Madden–Julian Oscillation, Geophys. Res. Lett, 41, 998–1004, doi:10.1002/2013GL058648, 2014.

Kar, J., Fishman, J., Creilson, J. K., Richter, A., Ziemke, J., and Chandra, S.: Are there urban signatures in the tropospheric ozone column products derived from satellite measurements?, Atmos. Chem. Phys., 10, 5213–5222, doi:10.5194/acp-10-5213-2010, 2010.

Koopmans, L. H.: The Spectral Analysis of Time Series, Academic Press, New York, 366 pp., 1974.

ACPD
15, 6373–6401, 2015

Lee, S., Shelow, D. M., Thompson, A. M., and Miller, S. K.: QBO and ENSO variability in temperature and ozone from SHADOZ, 1998–2005, J. Geophys. Res., 115, D18105, doi:10.1029/2009JD013320, 2010.

Lin, M., Horowitz, L. W., Oltmans, S. J., Fiore, A. M., and Fan, S.: Tropospheric ozone trends at Manna Loa Observatory tied to decadal climate variability, Nat. Geosci., 7, 136–143, doi:10.1038/NGEO2066, 2014.

Livesey, N. J., Read, W. G., Froidevaux, L., Lambert, A., Manney, G. L., Pumphrey, H. C., Santee, M. L., Schwartz, M. J., Wang, S., Cofield, R. E., Cuddy, D. T., Fuller, R. A., Jarnot, R. F., Jiang, J. H., Knosp, B. W., Stek, P. C., Wagner, P. A., and Wu, D. L.: EOS MLS Version 3.3 Level 2 data quality and description document, Tech. rep., Jet Propulsion Laboratory, available at: http://mls.jpl.nasa.gov/ (last access: 27 February 2015), Jet Propulsion Laboratory, Pasadena, CA, 2011.

Madden, R. A. and Julian, P. R.: Description of the 40–50 day oscillation in the zonal wind in the tropical Pacific, J. Atmos. Sci., 28, 702–708, doi:10.1175/1520-0469(1971)028<0702:DOADOI>2.0.CO;2, 1971.

Madden, R. A. and Julian, P. R.: Observations of the 40–50 day tropical oscillation – a review, Mon. Weather Rev., 122, 814–837, doi:10.1175/1520-0493(1994)122<0814:OOTDTO>2.0.CO;2, 1994.

Oman, L. D., Ziemke, J. R., Douglass, A. R., Waugh, D. W., Lang, C., Rodriguez, J. M., and Nielsen, J. E.: The response of tropical tropospheric ozone to ENSO, Geophys. Res. Lett., 38, L13706, doi:10.1029/2011GL047865, 2011.

Oman, L. D., Douglass, A. R., Ziemke, J. R., Rodriguez, J. M., Waugh, D. W., and Nielsen, J. E.: The ozone response to ENSO in Aura satellite measurements and a chemistry climate model, J. Geophys. Res., 118, 965976, doi:10.1029/2012JD018546, 2013.

Ragsdale, K. M., Barret, B. S., and Testino, A. P.: Variability of particulate matter (PM_{10}) in Santiago, Chile by phase of the Madden–Julian Oscillation (MJO), Atmos. Environ., 81, 304–310, doi:10.1016/j.atmosenv.2013.09.011, 2013.

Randel, W. J. and Thompson, A. M.: Inter-annual variability and trends in tropical ozone derived from SAGE II satellite data and SHADOZ ozonesondes, J. Geophys. Res., 116, D07303, doi:10.1029/2010JD015195, 2011.

Randel, W. J., Garcia, R. R., Calvo, N., and Marsh, D.: ENSO influence on zonal mean temperature and ozone in the tropical lower stratosphere, Geophys. Res. Lett., 36, L15822, doi:10.1029/2009GL039343, 2009.

ACPD
15, 6373–6401, 2015

Rienecker, M. M., Suarez, M. J., Gelaro, R., Ricardo Todling, Bacmeister, J., Liu, E., Bosilovich, M. G., Schubert, S. D., Takacs, L., Kim, G.-K., Bloom, S., Chen, J., Collins, D., Conaty, A., da Silva, A., Gu, W., Joiner, J., Koster, R. D., Lucchesi, R., Molod, A., Owens, T., Pawson, S., Pegion, P., Redder, C. R., Reichle, R., Robertson, F. R., Ruddick, A. G., Sienkiewicz, M., and Woollen, J.: MERRA – NASA's modern-era retrospective analysis for research and applications, J. Climate, 24, 3624–3648, doi:10.1175/JCLI-D-11-00015.1, 2011.

Strode, S. A., Rodriguez, J. M., Logan, J. A., Cooper, O. R., Witte, J. C., Lamsal, L. N., Damon, M., Steenrod, S. D., and Strahan, S. E.: Trends and variability in surface ozone over the United States, J. Geophys. Res., in review, 2014.

Sudo, K. and Takahashi, M.: Simulation of tropospheric ozone changes during 1997–1998 El Niño: meteorological impact on tropospheric photochemistry, Geophys. Res. Lett., 28, 4091–4094, doi:10.1029/2001GL013335, 2001.

Sun, W., Hess, P., and Tian, B.: The response of the equatorial tropospheric ozone to the Madden–Julian Oscillation in TES satellite observations and CAM-chem model simulation, Atmos. Chem. Phys., 14, 11775–11790, doi:10.5194/acp-14-11775-2014, 2014.

Thompson, A. M., Witte, J. C., Hudson, R. D., Guo, H., Herman, J. R., and Fujiwara, M.: Tropical tropospheric ozone and biomass burning, Science, 291, 5511, 2128–2132, doi:10.1126/science.291.5511.2128, 2001.

Trenberth, K. E.: The definition of El Nino, B. Am. Meteorol. Soc., 78, 2771–2777, doi:10.1175/1520-0477(1997)078<2771:TDOENO>2.0.CO;2, 1997.

van Donkelaar, A., Martin, R. V., Leaitch, W. R., Macdonald, A. M., Walker, T. W., Streets, D. G., Zhang, Q., Dunlea, E. J., Jimenez, J. L., Dibb, J. E., Huey, L. G., Weber, R., and Andreae, M. O.: Analysis of aircraft and satellite measurements from the Intercontinental Chemical Transport Experiment (INTEX-B) to quantify long-range transport of East Asian sulfur to Canada, Atmos. Chem. Phys., 8, 2999–3014, doi:10.5194/acp-8-2999-2008, 2008.

van der Werf, G. R., Randerson, J. T., Giglio, L., Collatz, G. J., Mu, M., Kasibhatla, P. S., Morton, D. C., DeFries, R. S., Jin, Y., and van Leeuwen, T. T.: Global fire emissions and the contribution of deforestation, savanna, forest, agricultural, and peat fires (1997–2009), Atmos. Chem. Phys., 10, 11707–11735, doi:10.5194/acp-10-11707-2010, 2010.

Zeng, G. and Pyle, J. A.: Influence of El Niño Southern Oscillation on stratosphere/troposphere exchange and the global tropospheric ozone budget, Geophys. Res. Lett., 32, L01814, doi:10.1029/2004GL021353, 2005.

ACPD
15, 6373–6401, 2015

Ziemke, J. R. and Chandra, S.: A Madden–Julian Oscillation in tropospheric ozone, Geophys. Res. Lett., 30, 2182, doi:10.1029/2003GL018523, 2003.

Ziemke, J. R., Chandra, S., Duncan, B. N., Froidevaux, L., Bhartia, P. K., Levelt, P. F., and Waters, J. W.: Tropospheric ozone determined from Aura OMI and MLS: evaluation of measurements and comparison with the Global Modeling Initiative's Chemical Transport Model, J. Geophys. Res., 111, D19303, doi:10.1029/2006JD007089, 2006.

Ziemke, J. R., Chandra, S., Schoeberl, M. R., Froidevaux, L., Read, W. G., Levelt, P. F., and Bhartia, P. K.: Intra-seasonal variability in tropospheric ozone and water vapor in the tropics, Geophys. Res. Lett., 34, L17804, doi:10.1029/2007GL030965, 2007.

Ziemke, J. R., Chandra, S., Oman, L. D., and Bhartia, P. K.: A new ENSO index derived from satellite measurements of column ozone, Atmos. Chem. Phys., 10, 3711–3721, doi:10.5194/acp-10-3711-2010, 2010.

Ziemke, J. R., Olsen, M. A., Witte, J. C., Douglass, A. R., Strahan, S. E., Wargan, K., Liu, X., Schoeberl, M. R., Yang, K., Kaplan, T. B., Pawson, S., Duncan, B. N., Newman, P. A., Bhartia, P. K., and Heney, M. K.: Assessment and applications of NASA ozone data products derived from Aura OMI/MLS satellite measurements in context of the GMI Chemical Transport Model, J. Geophys. Res. Atmos., 119, 5671–5699,doi:10.1002/2013JD020914, 2014.

ACPD
15, 6373–6401, 2015

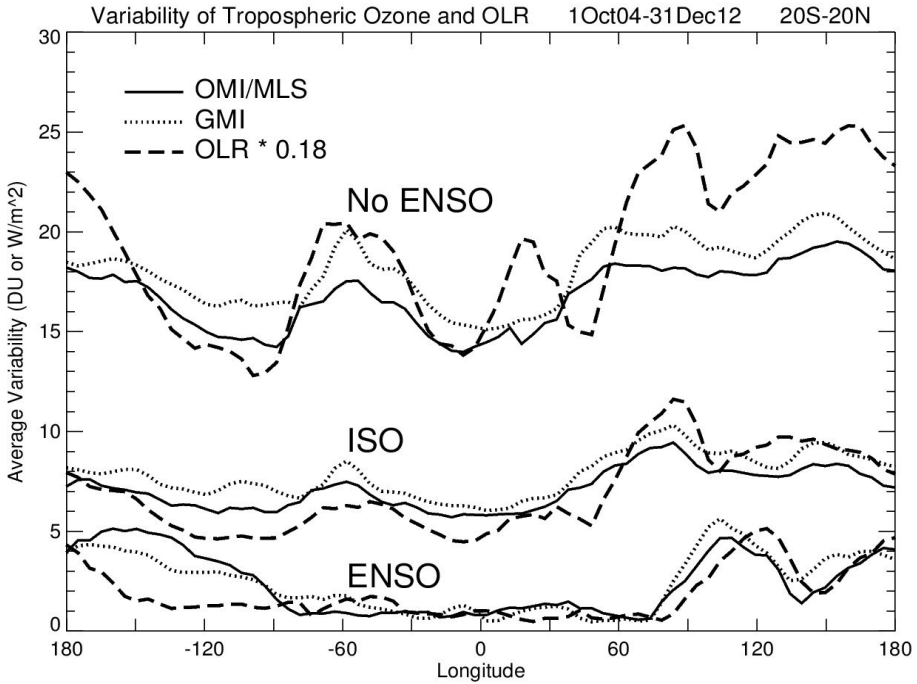

Figure 1. Variability in deseasonalized OMI/MLS daily tropospheric column ozone (solid curves), GMI CTM (dotted curves), and OLR (long dashed curves) for ENSO signal, intraseasonal oscillation (ISO) signals, and with ENSO signals removed (no ENSO). ISO curves involved band-pass filtering the time series for 25–65 day periods. OLR (units W m^{-2}) was multiplied by a factor of 0.18 for plotting with ozone. The plotted variability was calculated using amplitude of 2σ to estimate peak-to-peak change. The time record is 1 October 2004–31 December 2012 and all original time series were averaged over 20° S–20° N. The ENSO signals were extracted using the linear regression $T(t) = \beta \cdot \text{Nino34}(t-1) + \varepsilon(t)$, where T is original time series, t is day index, β is a derived constant, Nino34(t) is the Nino 3.4 ENSO index, and $\varepsilon(t)$ is the residual.

ACPD
15, 6373–6401, 2015

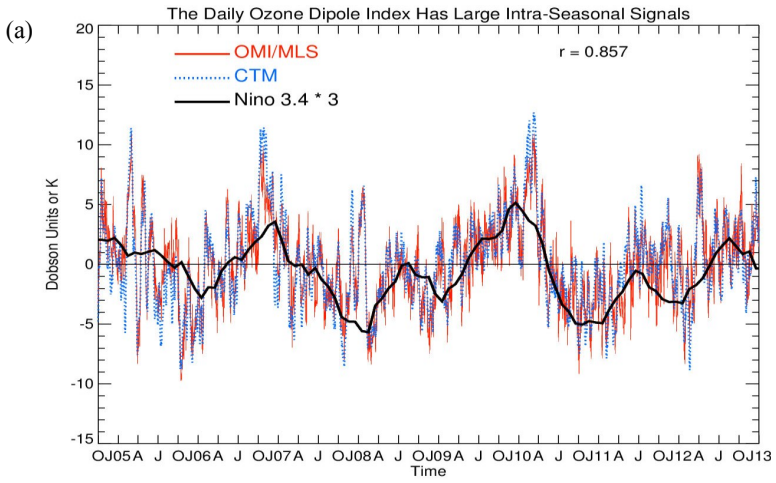

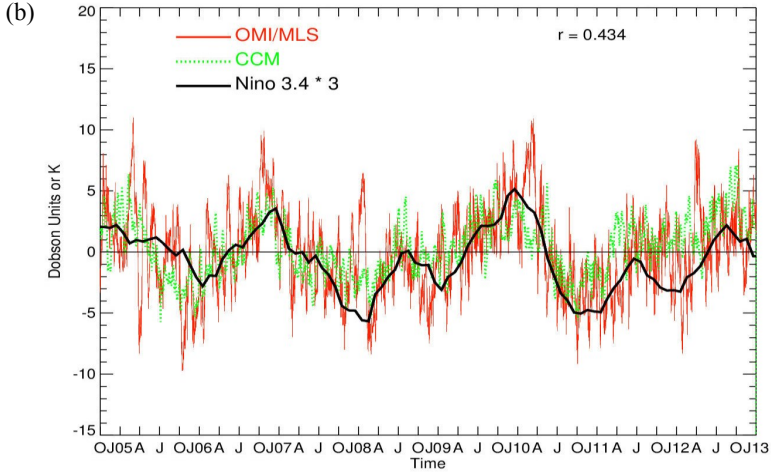

ACPD
15, 6373–6401, 2015

Tropospheric ozone variability in the tropics from ENSO to MJO and shorter timescales

J. R. Ziemke et al.

Figure 2. (a) Daily ODI (in Dobson Units) for OMI/MLS data (solid red curve) and CTM output (dotted blue curve). The monthly-mean Niño 3.4 ENSO index (thick black curve; units K and multiplied by 3 for plotting) is included for comparison with the two ODI time series. The ODI time series is derived by subtracting the eastern Pacific (15° S–15° N, 110–180° W) from western Pacific (15° S–15° N, 70–140° E) deseasonalized tropospheric column ozone. The correlation between the two daily ODI time series printed in the upper right of this figure is 0.857. **(b)** Same as **(a)** but with the CCM (dotted green curve) in place of CTM.

ACPD
15, 6373–6401, 2015

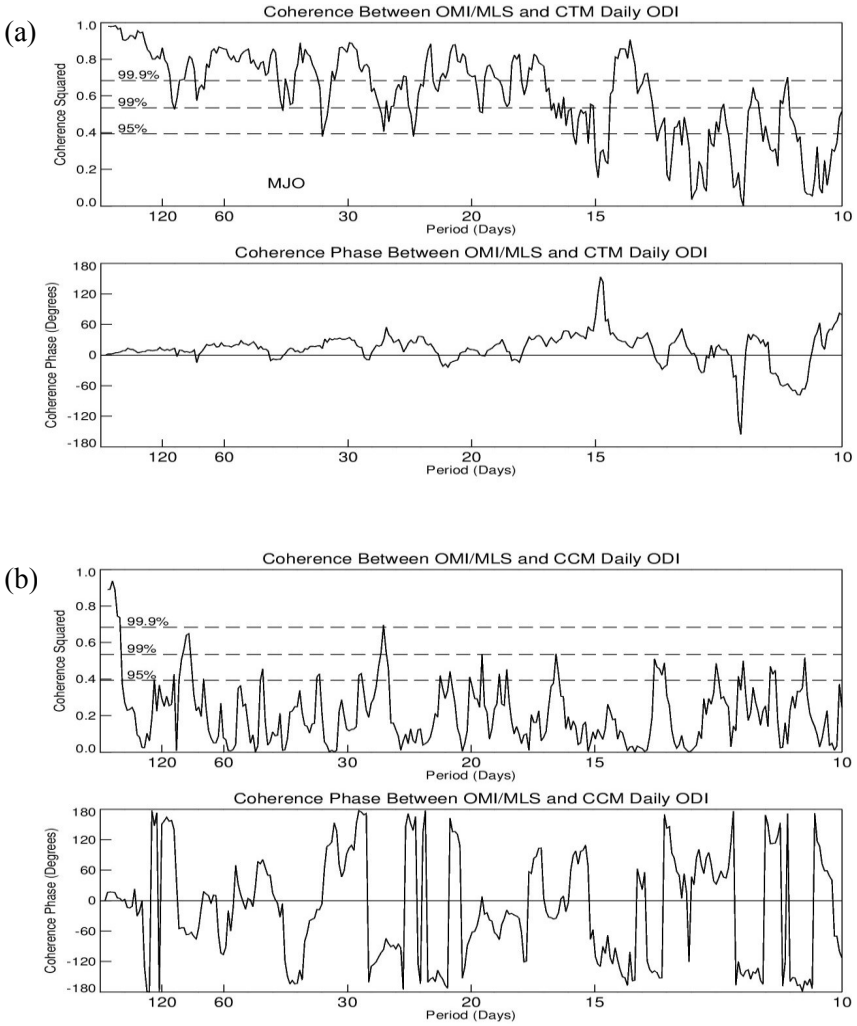

ACPD
15, 6373–6401, 2015

Tropospheric ozone variability in the tropics from ENSO to MJO and shorter timescales

J. R. Ziemke et al.

Figure 3. (a) Top panel: coherence-squared as function of frequency (periods in days shown) between OMI/MLS ODI and CTM ODI. Included are confidence levels for coherence-squared of 95 % (i.e., value of 0.393), 99 % (value of 0.536), and 99.9 % (value of 0.684). Bottom panel: coherence-phase in units of degrees. **(b)** Same as **(a)** but for the CCM instead of CTM. (See Appendix A for details of these statistical calculations.)

ACPD
15, 6373–6401, 2015

(a)

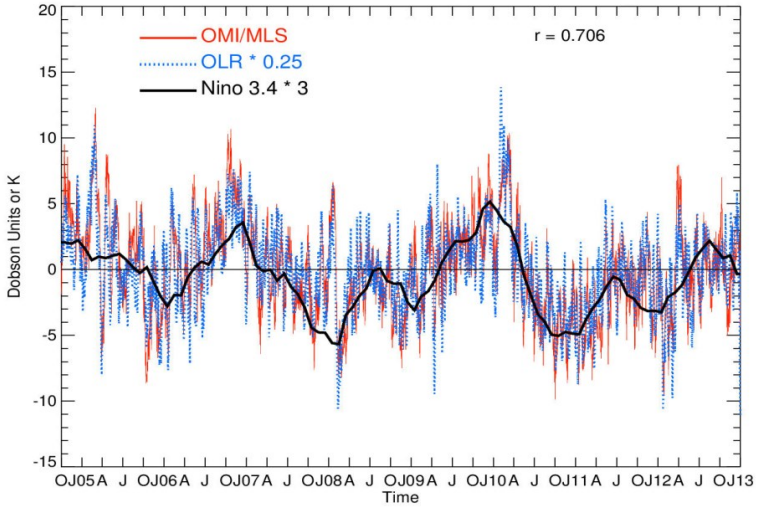

(b)

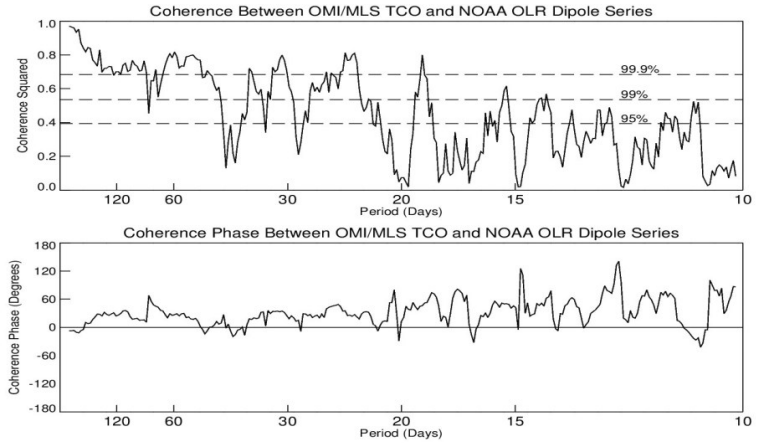

ACPD
15, 6373–6401, 2015

Tropospheric ozone variability in the tropics from ENSO to MJO and shorter timescales

J. R. Ziemke et al.

Figure 4. (a) Similar to Fig. 2a, except with calculated NOAA OLR dipole series (blue dashed curve) replacing the CTM ODI. OLR time series values have been divided by 4 for plotting with ozone. **(b)** Similar to Fig. 3a except for calculated coherence and coherence phase between the OMI/MLS ODI and OLR dipole time series in **(a)**.

ACPD
15, 6373–6401, 2015

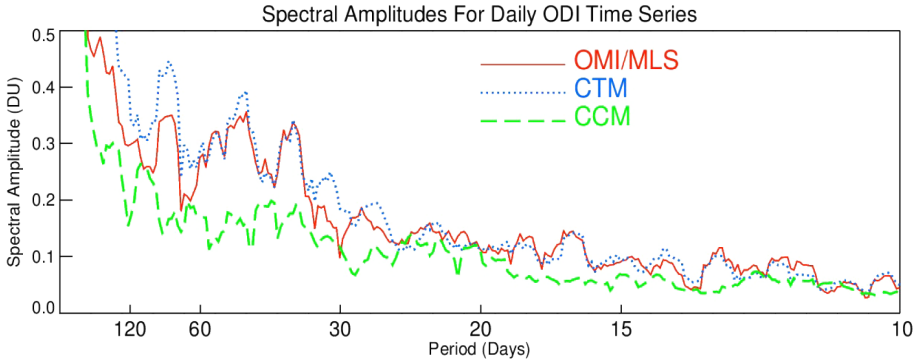

Figure 5. Calculated spectral amplitudes (in DU) as a function of frequency (periods in days shown) for the ODI calculated from the OMI/MLS data (red curve), CTM output (dotted blue curve), and CCM output (long dashed green curve). Spectral amplitude is defined as the square root of $\overline{c(\omega)^2 + s(\omega)^2}$, where c and s denote Fourier cosine and sine coefficients, ω is frequency and the over-bar denotes application of a smoothed spectral estimator. (See Appendix A for details of these calculations.)

ACPD
15, 6373–6401, 2015

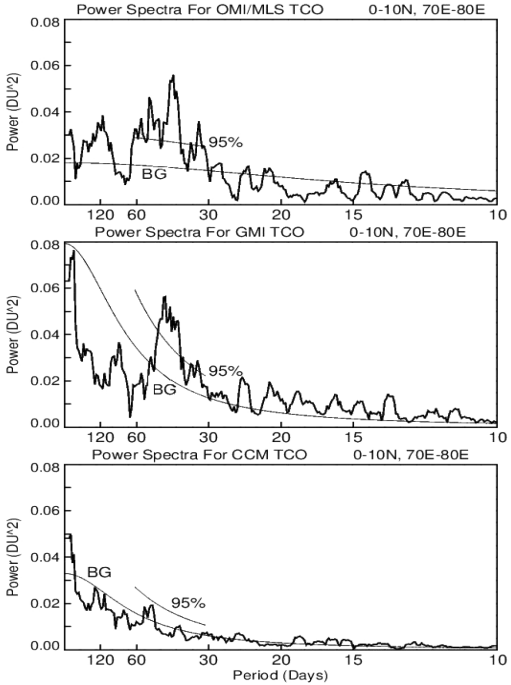

Figure 6. All three panels show calculated power spectra (in units of DU^2) of daily tropospheric column ozone time series averaged over a broad region of the tropical Indian Ocean (0–10° N, 70–80° E) where the MJO signal is statistically significant well above 95 % for OMI/MLS and the CTM. The top, middle, and bottom panels are for OMI/MLS data, CTM output, and CCM output, respectively. The power spectra are plotted vs. frequency with periods in days shown. A power spectrum is defined by $[\overline{c(\omega)^2 + s(\omega)^2}]/2$, where c and s denote derived Fourier cosine and sine coefficients, ω is circular frequency and the over-bar denotes application of a smoothed spectral estimator. Estimated background noise is denoted "BG" with 95 % confidence level is shown in each panel. (See Appendix A for details of these calculations.)

ACPD
15, 6373–6401, 2015

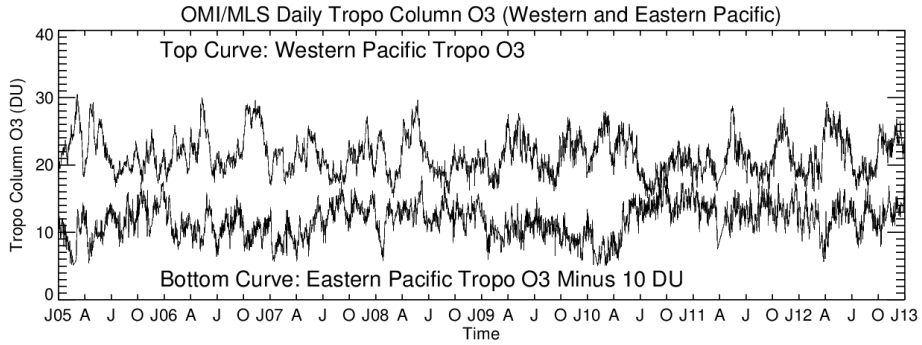

Figure A1. Top curve is daily tropospheric column ozone in Dobson Units from OMI/MLS averaged over the western Pacific (15° S–15° N, 70–140° E). Bottom curve is daily tropospheric column ozone in Dobson Units from OMI/MLS averaged over the eastern Pacific (15° S–15° N, 110–180° W). The bottom curve for eastern Pacific ozone was displaced by −10 DU for plotting.

ACPD
15, 6373–6401, 2015

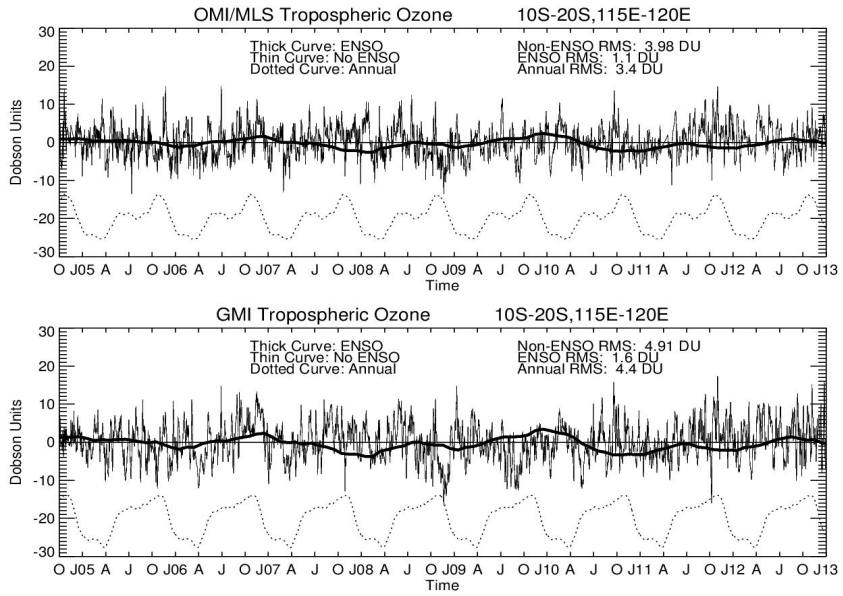

Figure A2. Top: OMI/MLS tropospheric column ozone (in Dobson Units) for the ENSO regression fit (thick curve) and non-ENSO components (thin curve). Also shown is the estimated annual cycle (dotted curve) which is offset from its average value by −20 DU for plotting. The chosen region for these time series is 10–20° S, 115–120° E and coincides with largest ENSO variability. Included in the panel are RMS values for the ENSO, non-ENSO, and annual cycle time series. ENSO signals were extracted from the deseasonalized time series using the linear regression $T(t) = \beta \cdot \text{Nino34}(t-1) + \varepsilon(t)$, where T is deseasonalized time series, t is day index, β is a derived constant, Nino34(t) is the Nino 3.4 ENSO index, and $\varepsilon(t)$ is the residual. Bottom: same as top panel except for the GMI CTM instead of OMI/MLS. The average annual cycle value for OMI/MLS TCO (GMI TCO) is 26.0 (31.2) DU; annual cycle minimum for OMI/MLS and GMI occurs in March–April with maximum in October–November. Correlation between the GMI and OMI/MLS non-ENSO time series is 0.703.

ACPD
15, 6373–6401, 2015